5. IMAGE DISSECTOR TUBE DATA PROCESSING

The image dissector tube data formed the main data stream for the Hipparcos mission. This detector assembly was situated behind the modulating grid and was capable of observing the light transmitted through a very small area of this grid, the so-called instantaneous field of view. This chapter describes the characteristics of the image dissector tube data and the reduction steps that prepared these data for further processing in the great circle reduction (as described in Chapter 9), the double star treatment (as described in Chapter 13) and the photometric treatment (as described in Chapter 14). The description of the reductions will use some information described in later chapters, most notably the results and description of the attitude reconstruction (as described in Chapter 7).

5.1. Description of the Measurements and Other Input Data

The Grid

A spherical glass surface, matching the curvature of optimal focus, was located in the focal plane of the telescope. The modulation grid, built up from 168 by 46 elements referred to as scan-fields, was engraved on this surface. Each scan-field contained 16 transparent lines. The method of engraving these lines meant that when projected orthogonally on a flat plane normal to the optical axis of the curved glass on which it was engraved, these grids are strictly rectangular, but while projected on the spherical surface of the focal plane, they are slightly distorted. These distortions could largely be compensated by expressing grid coordinates as direction cosines rather than angular displacements, as was done by NDAC, or as a two-dimensional fourth order model which includes simultaneously the actual grid distortion and the field-to-grid transformation, as done by FAST. Further (very small) corrections (the so-called medium-scale distortions) for the positions on the grid were determined and applied at the level of the phase determination during the great-circle reductions by NDAC (Section 10.3), and applied at each interlacing period according to the ground based measurements by FAST (Section 5.9).

The grid contained a small number of defects, identified during the pre-launch verification. Some of these defects were recognised in the data analysis in Utrecht (‘First Look’ analysis). The grid defects were accounted for in the FAST processing by rejecting data obtained close to a grid defect. No special measures were taken for this purpose by NDAC. The amount of data affected was very small.

The grid had a total of $168 \times 16 = 2688$ lines, with an average width of 3.13 μm and an average separation of 8.20 μm. More detailed specifications can be found in Chapter 2 of Volume 2. When projected on the sky, this gave a grid period of 1.2074 arcsec.

It was established early in the mission that the grid was oriented at an angle of 5 arcmin from the normal to the scanning circle. This was taken into account for the observations from mid-January 1990 onwards, but caused a small amount of degradation of the data accumulated during the first six weeks of the mission before this date.

The Instantaneous Field of View and Pointing

The instantaneous field of view (IFOV) allowed for the observation of objects within a small (30 arcsec diameter) area on the grid. It was directed towards the predicted position of a star by the satellite's on-board computer, using ground-based apparent-coordinate predictions and the satellite based real-time attitude determination (see Chapter 7). Thus, at times when problems occurred with the real-time attitude determination, the pointing of the IFOV was directly affected. Also, when *a priori* coordinates of an object were wrong by more than a few arcsec, then this also influenced the effective pointing. For this reason, many *a priori* coordinates were improved during the mission, initially using mainly results from the star mapper data reductions (see Chapter 6 and Volume 2, Chapter 8), and later using results of early sphere solutions.

The pointing of the IFOV was controlled with so-called coils currents, calibrated on-board the satellite and verified at ESOC at regular intervals during the mission (see also Volume 2, Chapters 5 and 10). This provided the 11×11 element coils current calibration matrix that made it possible for the data reduction consortia to reconstruct the IFOV pointing for every object observed. In the NDAC reductions the coils current calibration matrix was represented by a third order two-dimensional polynomial. The remaining standard deviation of the calibration data with respect to the fitted surface was of the order of 0.4 arcsec. The coils current step-size corresponded to 1.16 arcsec, which was therefore the highest pointing accuracy of the IFOV. The reduction software always selected the calibration nearest in time to the observations. In NDAC, coils currents supplied with observations were translated into positions on the grid and compared with positions based on reconstructed attitude (Chapter 7) and improved stellar positions. This allowed for rejection of data affected by bad pointing. Two selection criteria were used: a 7 arcsec limit, which provided very good quality data but also a relatively large loss of data, and a 10 arcsec limit, which gave a slight deterioration of the data but only very small losses. The final data were all reduced with the 10 arcsec limit. Figure 5.1 shows the IFOV pointing performance over the mission. Time intervals with relatively bad pointing were often associated with gyro-related attitude determination problems.

In FAST, the 11×11 coils current calibration matrix was extended by third order Lagrange interpolation formula to a 41×41 mesh of coils current values, each giving a pair of G and H coordinate values. This mesh was then inverted into a 41×41 mesh of G and H values giving the corresponding coils currents. Such a table was constructed for every orbit and then used by linear interpolation formulae to obtain G and H from the coils current values provided by ESOC for each star observed at mid-time of each observation frame.

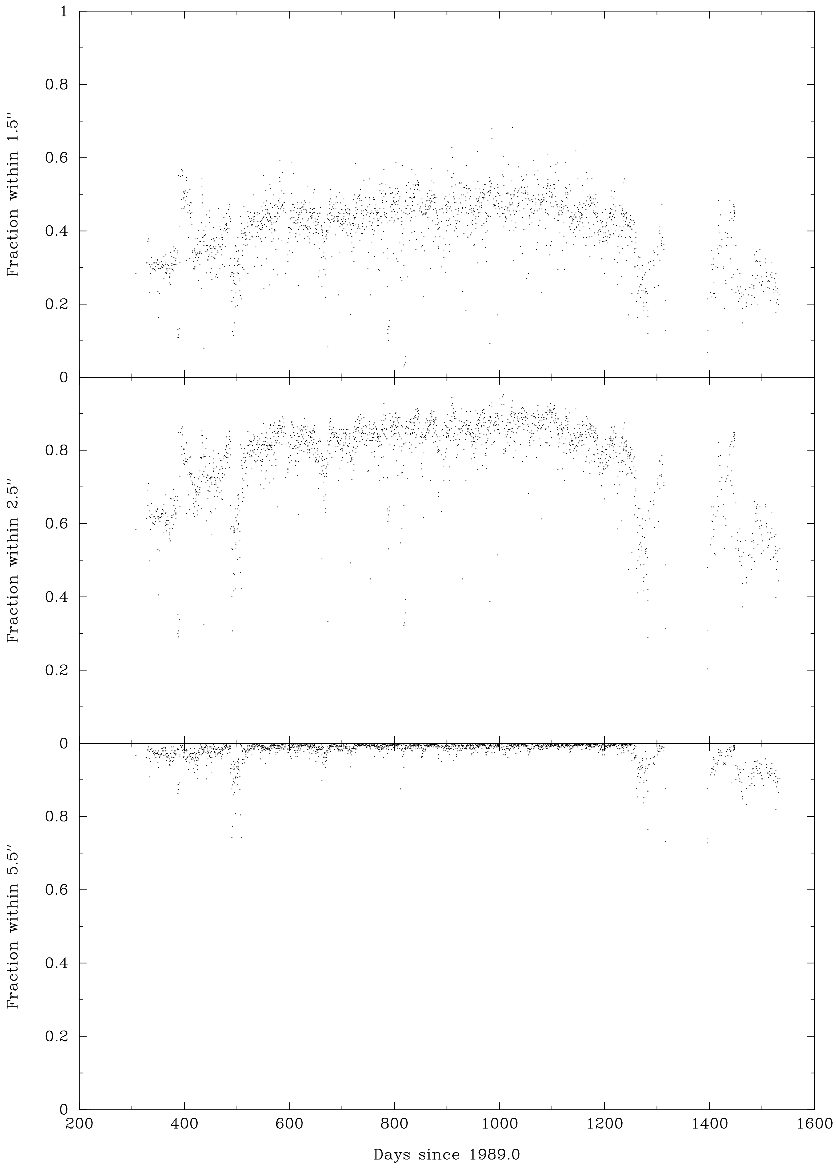

Figure 5.1. *The observed pointing accuracy of the IFOV over the mission. The graphs show the fraction of observations for which the reconstructed IFOV pointing was within the indicated radius from the actual position of the stellar image. Only observations within 9.5 arcsec of the reconstructed IFOV pointing were used. Those outside were associated with failures of the real-time attitude determination convergence.*

The sensitivity profile of the IFOV was calibrated by ESOC and showed that serious attenuation started at about 5 arcsec from its centre. The calibrated average IFOV is shown in Figure 5.2. There were variations with colour and with position in the field of view.

The sensitivity of the IFOV at a distance of 100 arcsec from the centre was still at a level of 0.04 per cent, allowing light from very bright stars to slightly disturb the measurements of fainter stars through the so-called ‘veiling glare’. As virtually all bright stars were also programme stars, this effect could be predicted, and veiling-glare corrections were applied by FAST. No veiling-glare corrections were applied by NDAC, where instead all image dissector tube transits were checked *a posteriori* for possible coincidences with other stellar images.

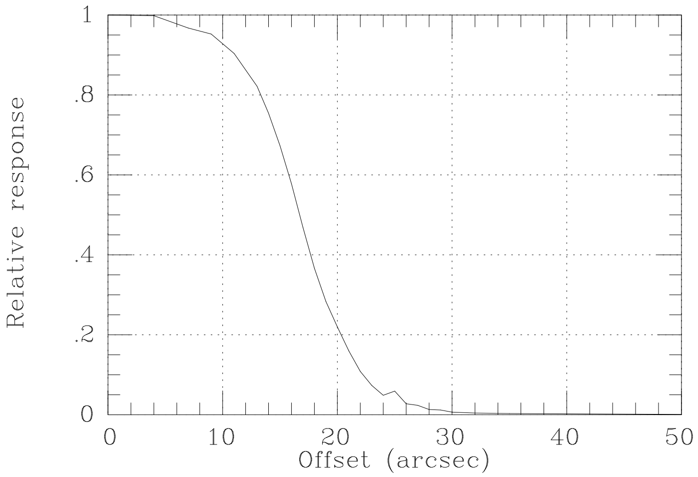

Figure 5.2. *The average instantaneous field of view profile.*

Observing Strategy

The integration time for a single image dissector tube observation (the sampling period) was $T_1 = 1/1200$ s. The observing strategy, i.e. the allocation of image dissector tube samples to the programme stars and the controlling of the instantaneous field of view pointing, was built on this unit (see Table 8.2). The image dissector tube data were processed in blocks of samples collected over an interval of 32/15 s, referred to as an observational frame ($T_4 = 2560T_1$). Within this time interval between one and ten stars could be observed quasi-simultaneously. The average number of programme stars in the $0\overset{\circ}{.}9 \times 0\overset{\circ}{.}9$ field was 4.8. The observational frame was split into 16 interlacing periods of 2/15 s ($T_3 = 160T_1$), during which every star would receive its designated fraction of observing time. The observing time was distributed in units of 8 sample periods (also referred to as 'slots', $T_2 = 8T_1$), mainly according to the brightness of the object to be observed and the competition for observing time from other objects. A 'slot' almost covered the passage across one grid period: at an average scan-velocity of 168.75 arcsec s^{-1} (equal to 360 arcsec per observational frame), the path-length of a stellar image over the grid during a 'slot' equalled 1.125 arcsec, just under the 1.2074 arcsec of the grid period.

When switching from one object to the next, a tiny but significant amount of time was lost from the first integration interval after repositioning. Every first sample in the first slot obtained immediately after a repositioning was therefore not used in the reductions. Special provisions were made for brighter stars entering or leaving the field, which were observed for only part of the observational frame in units of two 'slots' per interlacing period. These observations were referred to as 'partially observed stars', and have required special attention in the data reductions. Further details of the star observing strategy are given in Volume 2, Chapter 8.

Analogue Mode and Photon Counting Mode

Stars brighter than 1.5 mag were intended to be measured in analogue mode, fainter stars in photon-counting mode. It was discovered early in the mission that data obtained in the analogue mode was faulty due to a phase shift between the change-over

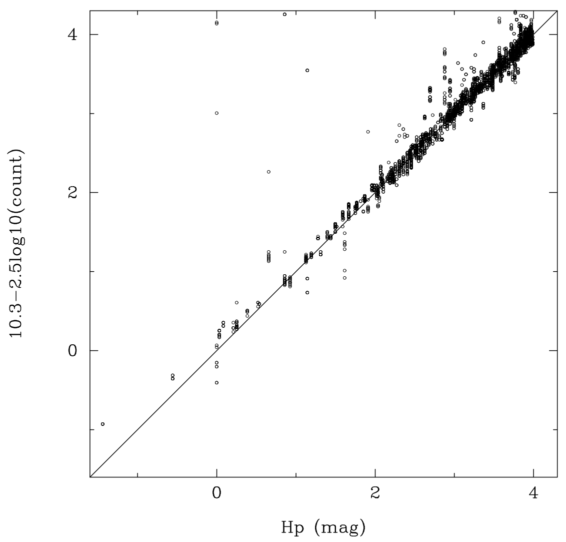

Figure 5.3. *Verification of the intensity transfer function (ITF), using data for the brightest stars. The diagonal line is the expected relation (apart from an offset) for properly decompressed counts. Only counts for Sirius, at -1.5 mag, were still affected by uncorrected saturation.*

from photon-counting to analogue mode (and back), and the switch of the instantaneous field of view between the stars concerned. Part of the data thus affected could still be reduced (this was only done by the NDAC consortium), but a proper calibration of the intensities obtained in analogue mode with respect to those obtained in photon-counting mode could not be obtained because of lack of data. The (very small) number of transits affected have not been included in the Hipparcos Epoch Photometry Annex, and concern only stars brighter than $Hp = 1.5$ with observations obtained before JD 2 447 925.0. It thus follows that all epoch photometry data presented in the Hipparcos Epoch Photometry Annex (HEPA, see Volume 1) were obtained in photon-counting mode, which means that some distortion of the signal could take place, primarily affecting the final photometric results of one or two of the brightest stars, due to saturation of the highest counts.

The Decompression of Photon Counts

The photon counts were compressed on-board the satellite using a semi-logarithmic scheme (see Volume 2, Chapters 3 and 9) to create a 1-byte integer in the range 0 to 255. A decompression law for the photon counts had been provided in the form of a table, relating the 255 possible compressed counts back to actual intensities. These relations were checked and partly re-calibrated, allowing for the effects of truncation and non-linearity. This was done early in the mission, using actual mission data. Figure 5.3 shows the relation for the decompressed counts and the stellar magnitudes for the brightest stars in the mission. Data from only a relatively short stretch of time could be used due to the changes in sensitivity of the image dissector tube tube detector (see Chapter 14). The selected counts were chosen very close to the maximum of the modulated signal, as based on the reconstruction of the phases. Before saturation set in, the noise introduced by the compression and decompression was well below the Poisson noise on the photon counts.

The Scanning Motion

The scanning motion of the satellite was never exactly around its z axis (see Chapter 7). Due to torques working on the satellite, accelerations existed around all three satellite axes, resulting in small amounts of rotation also around the x and y axes, as well as variations in the scan velocity around the z axis. The reduction process of the image dissector tube data used a reference position of the satellite at mid-time of the observational frame, and first and second derivatives with time of this position, to describe the position of the grid with respect to the position of a star at any time during the observational frame.

Quality Flag

A quality flag was added to the data by ESOC, based on the monitoring of the real-time attitude determination. However, during the first two years of the mission, this monitoring was unable to distinguish cases where only one field of view was properly converged in the attitude loop, and not the other. As a result, the use of this quality flag was limited, and did allow faulty data to enter early reduction stages. The quality flag was only used by FAST which, in addition, verified the relative positioning of the instantaneous field of view (using the coil currents) and of the stars, allowing rejection of most of the faulty observing frames in the photometric reduction. The effect on grid coordinates was negligible since this did not affect the modulation phases.

Information from the Catalogue

The star catalogue, initially a preliminary version of the Hipparcos Input Catalogue, provided initial positions, magnitudes and colours for the observed stars. The positions were important for the proper recognition of small scale distortions such as grid errors, and for a comparison between the pointing of the instantaneous field of view and the reconstructed position of the star on the grid. This catalogue was updated several times during the mission (see Volume 2, Section 8.3 and Table 8.3), first using additional ground-based data and later using star mapper data.

Magnitudes and colours were mainly important for the 'optical transfer function' calibration, described in Section 5.9, which allowed a distinction between single stars and double and multiple stars and were used in the photometric reductions and minor planet analysis.

5.2. The Signal Model

Five-Parameter Models

The image dissector tube photon counts N_k obtained for a star during an observational frame were described as a sequence of statistically independent and Poisson-distributed counts, having ideally a time-periodic expected value of $\mathrm{E}(N_k) \equiv I_k$. This modulated

Table 5.1. Relations between the parameters in Equation 5.4, 5.1 and 5.3.

[5.4]	[5.1]	[5.3]
β_1	b_1	$I_b + I_s$
β_2	$\sqrt{b_2^2 + b_3^2}$	$I_s M_1$
β_3	$\arctan(-b_3/b_2)$ $[+\pi]$	g_1
β_4	$\left((b_2^2 - b_3^2)b_4 + 2b_2b_3b_5\right)/(b_2^2 + b_3^2)^{3/2}$	$(M_2/M_1)\cos 2(g_1 - g_2)$
β_5	$\left((b_2^2 - b_3^2)b_5 - 2b_2b_3b_4\right)/(b_2^2 + b_3^2)^{3/2}$	$(M_2/M_1)\sin 2(g_1 - g_2)$

Table 5.2. Relations between the parameters in Equation 5.2, 5.1, 5.3 and 5.5.

[5.2]	[5.1]	[5.3]	[5.5]
	$\mathbf{a} = F_1(\mathbf{b})$		$\mathbf{a} = F_2(\mathbf{r})$
a_1	b_1	$I_b + I_s$	r_1
a_2	$\sqrt{b_2^2 + b_3^2}$	$I_s M_1$	r_2
a_3	$\arctan(-b_3/b_2)$ $[+\pi]$	g_1	r_3
a_4	$\sqrt{b_4^2 + b_5^2}$	$I_s M_2$	μr_2
a_5	$\arctan(-b_5/b_4)$ $[+\pi]$	$g_1 + g_2$	$r_3 + \nu$

signal was accurately represented by a first and second harmonic, five-parameter model (higher harmonics were not significant):

$$I_k(\mathbf{b}) = b_1 + b_2\cos p_k + b_3\sin p_k + b_4\cos 2p_k + b_5\sin 2p_k \qquad [5.1]$$

An equivalent form, separating intensity and phase parameters, was used by FAST:

$$I_k(\mathbf{a}) = a_1 + a_2\cos(p_k + a_3) + a_4\cos 2(p_k + a_5) \qquad [5.2]$$

which can also be given, expressed in parameters with direct physical interpretation, as:

$$I_k = I_b + I_s\left[1 + M_1\cos(p_k + g_1) + M_2\cos 2(p_k + g_1 + g_2)\right] \qquad [5.3]$$

In all cases the phases p_k were measured relative to the fiducial reference line of the main grid at mid-time of the observational frame. This reference line was positioned either halfway between slits 1344 and 1345 (NDAC) or in the middle of slit 1345 (FAST). In Equation 5.3, I_b represents the background signal (sky, radiation, dark current), I_s the signal intensity. g_1 is the actual phase of the first harmonic of the signal, relative to the fiducial reference line, at mid-frame time. M_1 and M_2 are the modulation coefficients for the first and second harmonics in the signal, while g_2 represents the phase difference between the first and second harmonic. The image dissector tube reductions aimed at the determination of $I_s + I_b$, g_1, g_2, M_1 and M_2, using the photon counts obtained during an observational frame.

An expression slightly different from Equation 5.2 was used by NDAC, and was referred to as the β-parameter solution:

$$I_k(\boldsymbol{\beta}) = \beta_1 + \beta_2\left[\cos(p_k + \beta_3) + \beta_4\cos 2(p_k + \beta_3) + \beta_5\sin 2(p_k + \beta_3)\right] \qquad [5.4]$$

where β_4 and β_5 were pure instrument parameters, describing together the amplitude ratio and the phase difference between the first and second harmonics. The relations between the parameters in Equations 5.4, 5.1 and 5.3 are given in Table 5.1 (NDAC reductions). The relations between Equations 5.2, 5.1, 5.3 and 5.5 are given in Table 5.2 (FAST reductions).

Three-Parameter Models

For single stars the amplitude ratio $\mu = a_4/a_2$ and phase difference $\nu = a_5 - a_3$ were a function of the colour of the object and the position of the measurement on the grid. Their calibration allowed the following representation of the signal:

$$I_k(\mathbf{r}) = r_1 + r_2\cos(p_k + r_3) + \mu r_2 \cos 2(p_k + r_3 + \nu) \qquad [5.5]$$

as used in the FAST reductions. In the NDAC reductions the three-parameter model was contained in Equation 5.4 through the calibration of β_4 and β_5. The calibration of these parameters is described in Section 5.9, dealing with the optical transfer function.

The Grid Phase of the Image Centre

The image centre was defined by the angular phase g_0, and was referred to as the reference phase. In the NDAC processing $g_0 = \beta_3$ was chosen, since β_3 was less sensitive to slight focal variations (which could be due to temperature variations) than was β_5, which was effectively the phase difference between the first and the second harmonic multiplied by the amplitude ratio of the second and first harmonics.

In FAST, g_0 was expressed as a linear combination of a_3 and a_5 (Equation 5.2):

$$g_0 = (1 - w)a_3 + wa_5$$

The choice of w which would minimise the variance of the combination would have been:

$$w = 4a_4^2/(a_2^2 + 4a_4^2)$$

However, a_2 and a_4 are not known *a priori* and the actual observed values may differ from one observation frame to another. Some constant value had to be taken also in order to facilitate subsequent processing of grid coordinates and present a unique reference throughout the reduction for multiple star reduction. The choice was, using the notation of Equation 5.3:

$$w = 4M_{20}^2/(M_{10}^2 + 4M_{20}^2) \qquad [5.6]$$

where the zero subscript indicates that these values of the parameters M_1 and M_2 were taken as constant. They were chosen, after evaluating calibrations made by the ‘First Look’ task, for a mean colour index equal to 0.5. The values chosen were $M_{10} = 0.70$ and $M_{20} = 0.20$, leading to the rounded value $w = 0.25$.

This choice had at least three advantages:

(1) to use the maximum amount of information present in a single star. Comparisons with other choices such as using only the first harmonic showed a significant improvement of the residuals in the great-circle reduction;

(2) in the case of double stars, although Equation 5.6 is not optimum, it provided on average more information than any other value for w, especially when M_1 is close to zero as may happen in some cases;

(3) tests made with ‘First Look’ results have shown that among all values of w, the one selected minimizes the rms of the great-circle reduction results.

5.3. Principles of the Image Dissector Tube Data Processing

The data processing in FAST and NDAC, although different in detail, proceeded along very similar lines. It aimed at estimating:

- the five photo-geometric parameters ($\mathbf{a}$ or $\boldsymbol{\beta}$), together with their respective covariance matrix ($\mathbf{A}$ or $\mathbf{B}_\beta$), to be used in subsequent double star and photometry processing;
- the three photo-geometric parameters of the single star model, to create a statistical test in charge of discriminating between single and multiple stars;
- the reference grid phase g_0 and its standard deviation, in NDAC referred to the fiducial reference line, in FAST referred to a reference slit number n_0, to be updated in subsequent processing.

The cornerstone of all image dissector tube processing was the following assumption: if the second order Fourier expansion given by Equation 5.1 (or its derived forms) exactly models the expected value I_k of the image dissector tube count N_k of a star, and the relative phases p_k are exactly known for each sample k, then the maximum likelihood estimate $\hat{\mathbf{b}}$, together with its estimated Cramér-Rao bound covariance matrix $\mathbf{B}$, tend asymptotically to be sufficient statistics of the image dissector tube samples of the observed star. The same assertion can be made for the alternative formulations leading to the parameter-covariance estimates $(\hat{\mathbf{a}}, \mathbf{A})$ and $(\hat{\boldsymbol{\beta}}, \mathbf{B}_\beta)$. The five parameters, e.g. $\mathbf{b}$ in Equation 5.1, could be estimated by maximizing the logarithm of the likelihood function:

$$\ln L(\mathbf{b}) = \sum_k [N_k \ln I_k(\mathbf{b}) - I_k(\mathbf{b}) - \ln(N_k!)] \qquad [5.7]$$

while the covariance of $\hat{\mathbf{b}}$ could be estimated as the negative inverse of the Hessian matrix, $\mathbf{B} = -[\partial^2 \ln L / \partial\mathbf{b}\partial\mathbf{b}']^{-1}$.

The assumption of sufficiency means that the estimation residuals tend to be a zero-mean white noise without any additional information on the modulated star signal. Consequently, any of the pairs $(\hat{\mathbf{b}}, \mathbf{B})$, $(\hat{\mathbf{a}}, \mathbf{A})$ or $(\hat{\boldsymbol{\beta}}, \mathbf{B}_\beta)$, corresponding to 20 independent parameters, could be used for further processing, replacing the original photon counts and providing considerable data compression. Furthermore, the constrained estimates $(\hat{\mu}, \hat{\nu})$ or $(\hat{\beta}_4, \hat{\beta}_5)$, corresponding to the three-parameter models, as well as the reference grid phase g_0, could also be computed from the compressed data $(\hat{\mathbf{a}}, \mathbf{A})$ or $(\hat{\boldsymbol{\beta}}, \mathbf{B}_\beta)$ without loss of precision.

Obviously, the modelling assumptions had to be carefully tested to ascertain that the estimated pair $(\hat{\mathbf{a}}, \mathbf{A})$ or $(\hat{\boldsymbol{\beta}}, \mathbf{B}_\beta)$ was statistically sufficient; this was done from the estimation residuals, using a pair of suitable statistical indices, detailed in Section 5.7.

Image Dissector Tube Processing Steps

The image dissector tube processing was partitioned in four steps (here described as done by FAST, the NDAC processing proceeded along very similar lines):

- computation of the relative phase p_k for each photon count N_k;

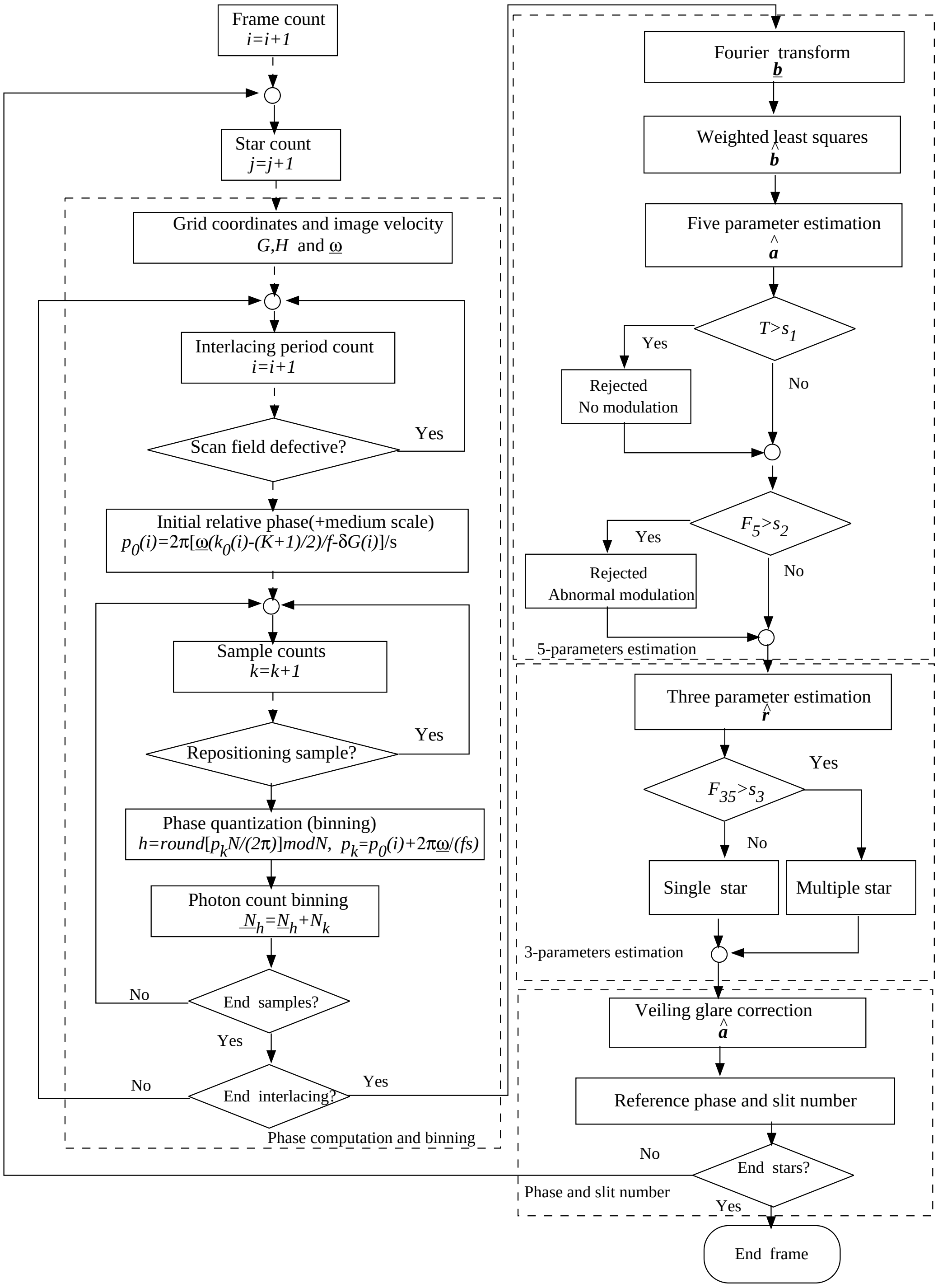

Figure 5.4 *Flow chart of the FAST image dissector tube processing.*

- maximum likelihood estimation of the five parameters **a** and model verification;
- Gauss-Markov estimation of the three parameters **r** and computation of the statistical index F_{35}, discriminating between single and multiple stars;
- veiling-glare correction of **a**, estimation of the reference grid phase g_0 and the slit number n_0.

The flow chart of the FAST image dissector tube processing is shown in Figure 5.4.

5.4. Calculation of the Relative Phases

The first step in the data processing required assigning relative modulation phases to the individual samples. Relative phases p_k for each sample could be determined very accurately from the position of the star on the grid (accuracy better than 1 arcsec), the angular rates of the satellite axes and the resulting scan-velocity, and the grid geometry, with or without taking into account the medium-scale distortions. The two data consortia used different approaches to the calculation of p_k, but the aim was the same: providing reliable phases for solving Equation 5.1 or its equivalent.

The Relative Phases of Samples as Derived by NDAC

Let **f**, **w** and **z** be orthogonal unit vectors with **f** the relevant viewing direction at the centre of the field, **w** the nominal scanning direction and **z** the normal to the viewing plane. The 'proper direction' to a star (Chapter 12) can then be expressed relative to the instrument as:

$$\mathbf{u} = v\mathbf{f} + w\mathbf{w} + z\mathbf{z} \qquad [5.8]$$

where w and z are the field coordinates (direction cosines) along the scan and transverse to the scan, respectively, and $v^2 + w^2 + z^2 = 1$. (w in Equation 5.8 should not be confused with the weights w defined in Equation 5.6).

For the ideal grid, the modulation phase varies linearly with the field coordinate w. In practice, the reference phase may be calculated as:

$$p_k = -\frac{2\pi}{s}(w - w_0) \qquad [5.9]$$

where w is the field coordinate of the image at the time of the kth sample, w_0 is the coordinate at the frame mid-time, and s is the grid period. The sign in Equation 5.9 is negative because w decreases with time when the satellite spins in the nominal sense (positive about **z**), whereas p_k is by definition an increasing quantity.

Neither w nor w_0 were known with much precision at the time of the image dissector tube data processing, mainly due to uncertainties of the order of 1 arcsec in the star coordinates. The field coordinates were, however, sufficiently well known and the incremental field coordinate $w - w_0$ could be calculated to within a few milliarcsec for the duration of an observation frame from the scanning velocity. The variations of w and z with time were evaluated on the assumption that the angular velocity vector direction, but not necessarily the speed, remained constant throughout the frame.

Let **h** denote the unit vector along the instantaneous axis of rotation of the satellite and **u** the unit vector to a star at arbitrary time t, relative to axes fixed in the satellite. Then:

$$\mathbf{u} = (\mathbf{h}'\mathbf{u})\mathbf{h} + (\mathbf{h}\times\mathbf{u})\times\mathbf{h} \tag{5.10}$$

Now let $\mathbf{u}_0$ be the star direction at the mid-time of the frame. Assuming that **h** remains fixed relative to the satellite, then $\mathbf{h}'\mathbf{u} = \mathbf{h}'\mathbf{u}_0$ and:

$$\mathbf{h}\times\mathbf{u} = \mathbf{h}\times\mathbf{u}_0\cos D + \mathbf{h}\times(\mathbf{h}\times\mathbf{u}_0)\sin D \tag{5.11}$$

where D is the angular phase of the spin at time t relative to mid-frame time. The direction of rotation about **h** is such that the relative spin phase decreases with time, i.e. $D = \psi_0 - \psi$, if ψ is the (increasing) attitude angle about the **z** axis. Combining Equations 5.10 and 5.11 gives:

$$\mathbf{u} = (\mathbf{h}'\mathbf{u}_0)\mathbf{h} + (\mathbf{h}\times\mathbf{u}_0)\times\mathbf{h}\cos D + \mathbf{h}\times\mathbf{u}_0\sin D \tag{5.12}$$

or:

$$\mathbf{u} = \mathbf{u}_0 + \mathbf{h}\times\mathbf{u}_0\sin D + \mathbf{h}\times(\mathbf{h}\times\mathbf{u}_0)(1-\cos D) \tag{5.13}$$

The direction of the instantaneous axis of rotation can be expressed as:

$$\mathbf{h} = h_1\mathbf{f} + h_2\mathbf{w} + h_3\mathbf{z} \tag{5.14}$$

where h_1 and h_2 depend on the field of view, but h_3 does not. Scalar multiplication of Equation 5.13 by **w** gives, by means of Equations 5.10 and 5.14:

$$w = w_0 + (h_3v_0 - h_1z_0)\sin D + [h_2h_1v_0 - (1-h_2^2)w_0 + h_2h_3z_0](1-\cos D) \tag{5.15}$$

where suffix zero denotes direction cosines at the mid-frame time. The coordinate z transverse to the scan is similarly obtained by scalar multiplication of Equation 5.13 by **z**:

$$z = z_0 + (h_1w_0 - h_2v_0)\sin D + [h_3h_1v_0 + h_3h_2w_0 - (1-h_3^2)z_0](1-\cos D) \tag{5.16}$$

The attitude determination gives the three components of the total inertial angular velocity vector of the satellite at each frame mid-time, relative to axes fixed in the satellite. Let ω be the total angular velocity at mid-frame time and $\dot\omega_3$ the component about **h** of the total angular acceleration; the spin phase at time t is then given by $D = -\omega t - \frac{1}{2}\dot\omega_3t^2$. Since v_0, w_0, z_0, h_1, h_2, h_3 are assumed to be constant for the observation of a given object in a frame, the required expressions for the variations of w and z are given by Equations 5.15 and 5.16.

The first stage in the analysis of the 2560 individual image dissector tube sample counts for an observing frame was to calculate the relative spin phase D for the first sample in each slot. Since all the samples in one slot came from the same star, the phase increment was evaluated at the mid-time of each slot, and used throughout the slot to calculate the reference phases of individual sample counts.

Denote by $\tau_n = (8n - 1287.5)T_1$ the time at the centre of the first sample in slot n, relative to the mid-frame time, where n goes from 1 to 320 over the frame. The relative spin phase D_n of the first sample of slot n is calculated from:

$$D_n = -\omega\tau_n - \frac{1}{2}\dot\omega_3\tau_n^2 \tag{5.17}$$

Since $\tau_{n+1} = \tau_n + T_2$, where $T_2 = 8T_1$ is the duration of one slot, the relative spin phase at slot $n+1$ can be written as:

$$D_{n+1} = D_n + \Delta D_n \tag{5.18}$$

where:

$$\Delta D_n = -(\omega + \dot{\omega}_3 \tau_n) T_2 - \frac{1}{2} \dot{\omega}_3 T_2^2 \qquad [5.19]$$

Also from Equation 5.19:

$$\Delta D_{n+1} = \Delta D_n - \dot{\omega}_3 T_2^2 \qquad [5.20]$$

The values of D_1 and ΔD_1 were evaluated at the start of the analysis of each frame, and the relative spin phases of the first samples of subsequent slots were obtained from the recurrence relations given by Equations 5.18, 5.19 and 5.20.

The calculation of reference phases was affected by inaccuracies in the field-to-grid transformation (i.e. in the assumed local value of the grid scale s), by variability inside the frame of the derivatives of the field coordinates, and by grid irregularities. The error contribution in the final estimation due to such inaccuracies was, however, negligible, as long as the specifications on angular velocity and field-to-grid transformation were met.

The methods described above were tested before launch using simulated data with and without photon noise. Noise levels introduced through the calculations of the relative phases were well below 0.1 mas, and therefore completely negligible.

Computation of the Relative Phases by FAST

Phase model: The estimate $\hat{p}_k$ of the relative phase p_k for each sample k was performed so as to guarantee that the global effect of the estimated errors $\hat{p}_k - p_k$ on the reference phase g_0 would be well below the dispersion due to the average photon noise in an observational frame, which was $\simeq 10$ mas. The budget of the phase errors $\hat{p}_k - p_k$ was constrained to contribute no more than a few milliarcsec noise.

The estimation procedure was based on the following model:

$$p_k = \frac{2\pi}{s} \left[\int_{t_0}^{t_k} \omega(\tau; \mathbf{p}) \mathrm{d}\tau + \delta\psi(t_k) + \delta p[G(t_k), H(t_k)] + \epsilon(t_k) \right] \mod 2\pi \qquad [5.21]$$

where the different terms have the following meaning:

- the integral describes the image motion across the grid from mid-frame time t_0 to sample-time t_k, modelled by a given parametric function for the apparent scan velocity $\omega(t; \mathbf{p}) = \mathrm{d}G(t)/\mathrm{d}t$ depending on the attitude vector $\mathbf{p}$. In practice this took into account the combination of the low-frequency components of the attitude motion and the large-scale distortions of the instrument. The integral was computed by assuming during the whole frame a uniform motion with a velocity $\bar{\omega} = \omega(t_0; \hat{\mathbf{p}})$ estimated from the attitude reconstruction (see Chapter 7) performed just before the image dissector tube data processing, and from the large-scale distortion calibrations provided by the 'First Look' task months in advance of the mass processing (see Chapter 4);
- the component $\delta\psi(t_k)$, usually referred to as jitter, described those motion components that could not be modelled by the previous parametric model, such as vibrations induced by thruster firings. However, the satellite design had reduced jitter to a negligible level of a few milliarcsec, except immediately following thruster firings. For this reason, the observation frame following the start of such an actuation was omitted from the data reduction;

- the term δp described the medium-scale distortions of the grid as provided by the on-ground calibrations as one value per scan-field (see also Sections 5.1 and 10.3). The correction values were set once per interlacing period, during which time a star would cross just over one scan-field;
- the term $\epsilon(t_k)$, modelled as a zero-mean white noise term, collected all the high-frequency irregularities, e.g. those resulting from phase quantization (binning).

Since the jitter component $\delta\psi(t_k)$ could be assumed negligible, the above modelling assumptions could be simplified to the following estimate:

$$\hat{p}_k = \frac{2\pi}{s}\left[(k - 1280.5)T_1\bar{\omega} + \delta p[G(\bar{t}_i), H(\bar{t}_i)]\right] \mod 2\pi, \quad k = k_1(i)\ldots k_2(i) \qquad [5.22]$$

where $k_1(i)$ and $k_2(i)$ are the first and last samples of the star within interlacing period i and $\bar{t}_i$ is the mid-time of the interlacing period; $T_1 = 1/1200$ s is the IDT sampling period.

Computation of scan velocity: The computation of the apparent scan velocity $\bar{\omega} = \mathrm{d}G(t)/\mathrm{d}t$ at the mid-frame time t_0 was based on the estimated attitude angles and rates and on the calibrated transformation from the field angles (η, ζ) to grid coordinates (G, H). The field-to-grid transformation was written:

$$G = \sin\eta\cos\zeta + \Delta G(\eta,\zeta), \quad H = \sin\zeta + \Delta H(\eta,\zeta) \qquad [5.23]$$

where the trigonometric terms account for the nominal transformation (Section 10.2) and the additional terms represent the large-scale distortions, in particular the rotation of the grid. Since the distortion terms had been calibrated, a pair of bi-cubic polynomials $g(\eta,\zeta;\mathbf{p}_1)$ and $h(\eta,\zeta;\mathbf{p}_2)$ could be used to compute G and H as:

$$G = \eta + g(\eta,\zeta;\mathbf{p}_1), \quad H = \zeta + h(\eta,\zeta;\mathbf{p}_2) \qquad [5.24]$$

after calibration of the 10-component vectors $\mathbf{p}_1$ and $\mathbf{p}_2$. Truncation to the third degree was justified since the fourth-degree terms were less than 1 mas at the field of view borders. Therefore, the apparent scan velocity was computed as:

$$\bar{\omega} = \dot{\eta}\left[1 + \frac{\mathrm{d}g(\eta,\zeta;\mathbf{p}_1)}{\mathrm{d}\eta}\right] + \dot{\zeta}\frac{\mathrm{d}g(\eta,\zeta;\mathbf{p}_1)}{\mathrm{d}\zeta} \qquad [5.25]$$

evaluated for $t = t_0$. During the data preparation (Chapter 4) the apparent coordinates $v(t_0)$, $r(t_0)$ in the great-circle frame (see also Section 9.2) had been calculated for each star observed in a frame. The three attitude angles $\psi(t_0)$, $\phi(t_0)$ and $\theta(t_0)$ were obtained from the attitude reconstruction (Chapter 7). The field angles (η, ζ) at mid-frame time t_0 were computed from these angles according to the equations below, where the time argument has been omitted for simplicity:

$$\begin{aligned} \eta &= \psi - v \pm \tfrac{1}{2}\gamma - \arcsin(\Delta/\cos\zeta) \\ \zeta &= \arcsin\{\cos r[\sin\theta\cos(\psi - v) + \sin\phi\cos\theta\sin(\psi - v)] + \sin r\cos\phi\cos\theta\} \end{aligned} \qquad [5.26]$$

where the upper and lower sign refers to the preceding and following field of view. The basic angle, as calibrated beforehand in the great-circle reductions of the 'First Look' task, including a correction for chromaticity according to the colour index of the star, is given by:

$$\gamma = \gamma_0 + [(V - I) - 0.5]\gamma_1$$

and a second-order correction in the small angles ϕ, θ and r can be expressed as:

$$\Delta = \frac{1}{2}\cos r\left[\sin\phi\sin 2\theta\cos 2(\psi - \nu) + \frac{\sin^2\phi\cos^2\theta - \sin^2\theta}{1+\cos\theta\cos\phi}\sin 2(\psi-\nu)\right]$$
$$+ \sin r[\sin\phi\cos\theta\cos(\psi-\nu) - \sin\theta\sin(\psi-\nu)]$$

Unlike η, the transversal field angle ζ depends to first order on these angles.

Similar formulae give the angular field rates from the attitude rates $\dot\phi(t_0)$, $\dot\theta(t_0)$ and $\dot\psi(t_0)$ also provided by the attitude reconstruction (Chapter 7). They were simplified by assuming (without degradation of accuracy) that the rate $\dot\psi(t_0)$ of the FAST scan angle was equivalent with the inertial rate around the third axis:

$$\dot\eta = \cos\phi\cos\theta\left[\dot\psi + \frac{\dot\theta\sin\phi + \dot\phi\sin\theta}{1+\cos\phi\cos\theta}\right] - \dot\theta\sin\phi$$
$$+ \tan\zeta\left[\sin(\psi-\nu)\left(\dot\theta\cos\phi - \dot\psi\sin\phi\cos\theta\right) - \cos(\psi-\nu)\left(\dot\phi - \dot\psi\sin\theta\right)\right]$$
$$\dot\zeta = \sin(\psi-\nu)\left(\dot\phi - \dot\psi\sin\theta\right) + \cos(\psi-\nu)\left(\dot\theta\cos\phi - \dot\psi\sin\phi\cos\theta\right) \qquad [5.27]$$

In their application, these formulae were computed through sufficiently accurate power expansions in the small angles ϕ, θ, and r.

5.5. Binning Techniques

At the time of the development and early implementation of the data reduction software, it was essential to look for ways of limiting the time spent on the processing of the 1200 image dissector tube samples received every second. Both data reduction consortia opted for a binning strategy, reducing the main processing tasks by a very considerable factor in both computing time and complexity.

The binning strategy assigns a reference phase p_i to all samples with phases p_k falling in a phase interval $p_i - \mathrm{d}p$ to $p_i + \mathrm{d}p$. With $p_k = p_i + \delta p_{k|i}$, and n_i samples falling in bin i, the expected count in bin i can be expressed as a modification of Equation 5.1:

$$\frac{1}{n_i}\sum N_{k|i} = b_1 + b_2\frac{1}{n_i}\left(\cos p_i\sum\cos\delta p_{k|i} - \sin p_i\sum\sin\delta p_{k|i}\right)$$
$$+ b_3\frac{1}{n_i}\left(\sin p_i\sum\cos\delta p_{k|i} + \cos p_i\sum\sin\delta p_{k|i}\right)$$
$$+ b_4\frac{1}{n_i}\left(\cos 2p_i\sum\cos 2\delta p_{k|i} - \sin 2p_i\sum\sin 2\delta p_{k|i}\right)$$
$$+ b_5\frac{1}{n_i}\left(\sin 2p_i\sum\cos 2\delta p_{k|i} + \cos 2p_i\sum\sin 2\delta p_{k|i}\right) \qquad [5.28]$$

The advantage of the binning arises from the δp_k being small, allowing approximations to be made for the $\sin\delta p_{k|i}$ etc., and from the fact that the p_i values remain constant, and therefore need to be calculated only once for all transits.

Two different implementations were used: the FAST consortium applied a strategy using 64 bins, and neglected the effect of δp_k, in which case binning corresponded to a quantization of the relative phase. It was estimated that the error on the relative phase p_k resulting from the binning should be less than $\simeq$ 10 mas, in which case the quantization effects on the grid phase estimate would be negligible with respect to the photon noise. The quantization noise σ_q for l bins was given by:

$$\sigma_q = \frac{s}{2\sqrt{3}l} \qquad [5.29]$$

where s is the grid-period of 1.2074 arcsec. For $l > 35$ it follows that $\sigma_q < 10$ mas. l was rounded up to the nearest power of 2, i.e. $l = 64$, giving $\sigma_q = 5.5$ mas and a noise contribution to the grid phase estimates less than 0.5 mas.

NDAC performed a substantial number of simulations and tests with various binning strategies, using both noise-free and Poisson-noise simulated data. The results of these tests showed that a substantial reduction in computing time without any significant loss of accuracy could be obtained using $l = 12$ bins and carrying along up to second order corrections for δp_k. The noise contribution to the phase estimates resulting from the binning this way, was less than 0.2 mas.

In the FAST approximation Equation 5.28 reduces to Equation 5.1, with p_k being replaced by the nearest p_i and $\mathcal{N}_i = \sum N_{k|i}$ being the total count per bin. In the NDAC approximation the equations obtained are:

$$\begin{aligned}
\frac{1}{n_i}\sum N_{k|i} = b_1 &+ b_2\frac{1}{n_i}\left(\cos p_i \sum(1 - \frac{1}{2}\delta p_{k|i}^2) - \sin p_i \sum \delta p_{k|i}\right) \\
&+ b_3\frac{1}{n_i}\left(\sin p_i \sum(1 - \frac{1}{2}\delta p_{k|i}^2) + \cos p_i \sum \delta p_{k|i}\right) \\
&+ b_4\frac{1}{n_i}\left(\cos 2p_i \sum(1 - 2\delta p_{k|i}^2) - \sin 2p_i \; 2\sum \delta p_{k|i}\right) \\
&+ b_5\frac{1}{n_i}\left(\sin 2p_i \sum(1 - 2\delta p_{k|i}^2) + \cos 2p_i \; 2\sum \delta p_{k|i}\right) \qquad [5.30]
\end{aligned}$$

This no longer required repeated trigonometric calculations, as these calculations were the same for each transit.

Critical Binning Conditions

For certain values of the scan-velocity the relative grid phases p_k would assume only a limited number of different values. At nominal scan velocity (168.75 arcsec s^{-1}), the phase shift from one sample to the next was $41\overset{\circ}{.}92$. At a scanning speed of 170.456 arcsec s^{-1}, the phase shift to the next sample was $42\overset{\circ}{.}35$, which meant that the phase shifts of 17 samplings fitted in exactly 2 complete modulation cycles. Similar situations happened for scan velocities of 173.866 arcsec s^{-1} (25 samplings in 3 cycles) and 167.178 arcsec s^{-1} (26 samplings in 3 cycles).

In the case of 64 bins without phase correction, this left a large number of bins unoccupied, and could cause systematic differences between assumed bin-phases and actual mean bin-phases. The latter effect was, however, small with respect to other sources of noise, most notably the Poisson noise on the photon counts.

The scan velocity was changing continuously, and a resonance situation similar to that described above would normally not persist over more than a few frames. No measures were taken to remedy these phenomena by FAST, while in NDAC they were implicitly taken care of in the normal reductions. In FAST, the statistical index T (described later) was able to detect a non-negligible bias in the grid phase, for example due to resonances.

5.6. Solution of the Binned Equations

Five-Parameter Estimation by FAST

The parameter estimation aimed at performing the maximum likelihood estimation of the five-parameter model (Equation 5.2). The solution equation was obtained by looking for stationary points of the maximum likelihood functional (Equation 5.7):

$$\frac{\partial \ln L}{\partial \mathbf{a}} = \sum_k \left(\frac{N_k - I_k(\mathbf{a})}{I_k(\mathbf{a})} \frac{\partial I_k(\mathbf{a})}{\partial \mathbf{a}} \right) = 0 \qquad [5.31]$$

Equation 5.31 is non-linear in $\mathbf{a}$, but a unique asymptotic solution exists if the model were identifiable and error free. Under such assumptions, the above equations could be interpreted as the solution of a Gauss-Markov estimation of $\mathbf{a}$, performed on the zero-mean uncorrelated residuals $e_k = N_k - I_k(\mathbf{a})$, having variance equal to $I_k(\mathbf{a})$. However, since the variance $I_k(\mathbf{a})$ depended on the unknown $\mathbf{a}$, the maximum likelihood could only be solved by iterating the Gauss-Markov estimation and by disposing of a suitable starting estimate of $I_k(\mathbf{a})$. On the other hand, if I_k were linear in the parameters as it is in Equation 5.1, then the Gauss-Markov estimator should correspond to weighted least-squares.

These considerations led to the following procedure:

(1) estimation of $\mathbf{b}$ by Fourier transforming the binned counts $\mathcal{N}_i$, providing a first estimate $\tilde{\mathbf{b}}$;

(2) weighted least-squares estimation of $\mathbf{b}$, given the estimated variances $I_k(\tilde{\mathbf{b}})$, hence providing the pair $(\hat{\mathbf{b}}, \mathbf{B})$ behaving like a sufficient statistic (even in the presence of veiling-glare);

(3) non-linear transformation from the pair $(\hat{\mathbf{b}}, \mathbf{B})$ to the pair $(\hat{\mathbf{a}}, \mathbf{A})$; in the course of this transformation it would have been possible to eliminate the biasing effect of the veiling-glare, as will be shown later on. In fact, the veiling-glare correction was performed just at the end of the image dissector tube processing;

(4) verification of the model hypotheses through statistical tests.

The Fourier transformation of the binned counts $\mathcal{N}_i$ used the equations:

$$\begin{aligned}
\tilde{b}_1 &= \frac{1}{l} \sum_{i=0}^{l-1} \mathcal{N}_i \\
\tilde{b}_2 &= \frac{2}{l} \sum_{i=0}^{l-1} \mathcal{N}_i \cos(2\pi i/l), \quad \tilde{b}_3 = \frac{2}{l} \sum_{i=0}^{l-1} \mathcal{N}_i \sin(2\pi i/l) \qquad [5.32] \\
\tilde{b}_4 &= \frac{2}{l} \sum_{i=0}^{l-1} \mathcal{N}_i \cos(4\pi i/l), \quad \tilde{b}_5 = \frac{2}{l} \sum_{i=0}^{l-1} \mathcal{N}_i \sin(4\pi i/l)
\end{aligned}$$

The second estimation step also took advantage of the binning, by reducing the number of observation equations to a fixed number ($l = 64$) of the following form:

$$\mathbf{u}_i' \mathbf{b} + e_i = \mathcal{N}_i, \quad i = 0 \ldots l-1 \qquad [5.33]$$

where $\mathbf{u}_i = [\,1\ \cos(2\pi i/l)\ \sin(2\pi i/l)\ \cos(4\pi i/l)\ \sin(4\pi i/l)\,]'$ is the vector of coefficients for bin i. The variance of the residual e_i was assumed to be $\sigma_i^2 = (l/m)I_i(\tilde{\mathbf{b}})$, with m being the total number of samples used. By collecting the l rows in Equation 5.33 in matrix form, $\mathbf{Ub} + \mathbf{e} = \mathbf{N}$, the weighted least-squares estimate was obtained as:

$$\hat{\mathbf{b}} = (\mathbf{U}'\mathbf{S}^{-1}\mathbf{U})^{-1}\mathbf{U}'\mathbf{S}^{-1}\mathbf{N} \qquad [5.34]$$

where $\mathbf{S}$ is the diagonal covariance matrix of $\mathbf{e}$.

The binning further simplified the computation of the (symmetric) Gram matrix $\mathbf{G} = \mathbf{U}'\mathbf{S}^{-1}\mathbf{U}$. 12 of the 15 different elements in $\mathbf{G}$ could be expressed as linear combinations of the first three elements:

$$g_{11} = \frac{m}{l}\sum_{i=0}^{l-1}\frac{1}{I_i(\tilde{\mathbf{b}})}, \quad g_{12} = \frac{m}{l}\sum_{i=0}^{l-1}\frac{\cos(2\pi i/l)}{I_i(\tilde{\mathbf{b}})}, \quad g_{13} = \frac{m}{l}\sum_{i=0}^{l-1}\frac{\sin(2\pi i/l)}{I_i(\tilde{\mathbf{b}})} \qquad [5.35]$$

By collecting the combinations of these three independent terms into a 12-element vector $\boldsymbol{\gamma}$ and the twelve remaining elements of $\mathbf{G}$ into a vector $\mathbf{g}$, a linear set of twelve equations results:

$$\boldsymbol{\gamma} = \mathbf{Hg} \qquad [5.36]$$

the non-zero elements of which are detailed in the following equation:

$$\begin{bmatrix} m - b_1g_{11} - b_2g_{12} - b_3g_{13} \\ -b_3g_{12} + b_2g_{13} \\ 0 \\ g_{11} \\ 0 \\ -b_1g_{12} \\ g_{13} \\ -b_1g_{13} \\ g_{12} \\ 0 \\ g_{11} \\ 0 \end{bmatrix} = \begin{bmatrix} b_4 & b_5 & & & & & & & & & & \\ 2b_5 & -2b_4 & & & & & & & & & & \\ & -1 & 2 & & & & & & & & & \\ & & & 1 & 1 & & & & & & & \\ -1 & & & 1 & -1 & & & & & & & \\ & & b_3 & b_2 & & b_4 & b_5 & & & & & \\ & & & & & & 1 & -1 & & & & \\ & & b_2 & & b_3 & & & b_4 & b_5 & & & \\ & & & & & 1 & & & 1 & & & \\ b_1 & & & & b_2 & & b_3 & & & b_4 & b_5 & \\ & & & & & & & & & 1 & & 1 \\ & b_1 & & & & b_2 & & b_3 & & & b_4 & b_5 \end{bmatrix} \begin{bmatrix} g_{14} \\ g_{15} \\ g_{23} \\ g_{22} \\ g_{33} \\ g_{24} \\ g_{25} \\ g_{34} \\ g_{35} \\ g_{44} \\ g_{45} \\ g_{55} \end{bmatrix}$$

$$[5.37]$$

This system can be easily solved for the unknown $\mathbf{g} = \mathbf{H}^{-1}\boldsymbol{\gamma}$ by exploiting the quasi-triangularity (Hessenberg form) of the matrix $\mathbf{H}$. The six rows with numerical coefficients, corresponding to the entries g_{22}, g_{23}, g_{25}, g_{33}, g_{35} and g_{45}, arose from trigonometric equalities; the six rows having coefficients equal to the elements of $\mathbf{b}$ arose from the weighted averaging of trigonometric functions sampled at regular steps.

Five-Parameter Estimation by NDAC

Each bin contributed one observation equation for the solution of the parameters b_1 to b_5. Each observation equation was given a weight according to the total count $\sum N_{k|i}$ in the bin:

$$W_i = \frac{n_i}{1 + \sum N_{k|i}} \qquad [5.38]$$

The addition of one in the denominator prevented an infinite weight for $\sum N_{k|i} = 0$. It can also be derived from an estimation of the most likely distribution to which an observed count belongs: when a total count of zero is observed, the most likely underlying distribution would have an expected value of one. Thus, in the NDAC

Table 5.3. Definitions of astrometric and photometric parameters used in FAST and NDAC.

Parameter	NDAC	FAST
‘dc’ photometry	β_1	$a_1 - I_b$
‘ac’ photometry	β_2	$(M_{10}a_2 + M_{20}a_4)/(M_{10}^2 + M_{20}^2)$
Reference phase	β_3	$(1 - w)a_3 + wa_5$

solution the only differences with treating every sampling on its own were the weight applied and the (very small) approximation of the reference phase. Because only twelve bins were used, the total number of samples per bin was usually not very low, and provided a reasonable estimate of the expected variance in a bin.

Transformation of the Solution

The sufficient statistics $(\hat{\mathbf{b}}, \mathbf{B})$ provided by the Gauss-Markov estimator were at the end transformed without degradation into the statistics $(\hat{\mathbf{a}}, \mathbf{A})$, defined by Equation 5.2 for FAST, or $(\hat{\boldsymbol{\beta}}, \mathbf{B}_\beta)$, defined by Equation 5.4 for NDAC. The transformation of the parameter vectors was made according to Table 5.1 and 5.2. The transformation of $\mathbf{B}$ to $\mathbf{B}_\beta$ was made by means of the Jacobian $\mathbf{J} = \partial\boldsymbol{\beta}/\partial\mathbf{b}'$ according to:

$$\mathbf{B}_\beta = \mathbf{JBJ}' \qquad [5.39]$$

and a corresponding equation was used to calculate $\mathbf{A}$.

The transformations from $\hat{\mathbf{b}}$ to $\hat{\boldsymbol{\beta}}$ (or $\hat{\mathbf{a}}$) led to biases in the amplitude estimates due to accumulation of squared errors. This was most noticeable for fainter stars, where the statistical correction led to an increase in the noise level on the transformed values. In particular, the correction to be subtracted from $\hat{\beta}_2$ was given by:

$$\Delta\beta_2 = (\sigma_2^2 + \sigma_3^2)/2\hat{\beta}_2 \qquad [5.40]$$

where σ_2 and σ_3 are the estimated errors on $\hat{b}_2$ and $\hat{b}_3$ respectively. Typical corrections amounted to a few per cent for the faintest stars, and negligible corrections for brighter stars.

The Photometric Parameters

The final solution, expressed as either Equation 5.2 or Equation 5.4 provided the input for the further processing of the photometric data. The two consortia made slightly different choices here: NDAC opted for simple parameters directly obtained from the zero level and first harmonic Equation 5.4, while FAST used combined information from the first and second harmonics for both the phase estimate used in the great-circle reductions and the ‘ac’ component used in the photometric reductions. The parameters, as used by the two groups, are summarised in Table 5.3, where M_{10} and M_{20} stand for the predicted modulation coefficients as derived from the optical transfer function calibration described in Section 5.9 and w was defined in Equation 5.6.

5.7. Statistical Tests of the Five-Parameter Solution

Two test parameters were derived at this stage: F and T. The first of these, F, tested the null hypothesis that no modulation was present in the signal, in other words, that the observed photon counts collected for a transit were a stationary Poisson white noise; hence F should appear significant when the photon-counts were sufficiently modulated. The second of these, T, tested the null hypothesis that the residuals left after application of the five-parameter model represented a zero-mean stationary white noise. Hence, T should appear significant when the residuals were modulated (failure of the 5-parameter model) or the original photon-counts were not Poisson distributed. The tests were carried out on the binned counts.

The Index *T*

In NDAC, a χ^2 value for the T statistic was derived for the binned mean counts, assuming them to be represented by $I_k(\hat{\mathbf{b}})$:

$$\chi^2 = \sum_{i=1}^{l} \frac{\left[(1/n_i)\sum N_{k|i} - I_k(\hat{\mathbf{b}})\right]^2}{(1/n_i)\sum N_{k|i}} \qquad [5.41]$$

where $l = 12$ is the number of bins and where the denominator represents the expected variance of the residuals. The χ^2 value was transformed into a pseudo-Gaussian variable, which under the null hypothesis should have a unit-normal distribution:

$$T = \sqrt{\frac{9d}{2}}\left[\left(\frac{\chi^2}{d}\right)^{1/3} - 1 + \frac{2}{9d}\right] \qquad [5.42]$$

where d is the number of degrees of freedom, normally equal to $l - 5 = 7$ for the T statistic. Transits for which $|T| > 4.0$ were flagged in the Hipparcos Catalogue Epoch Photometry Annex as suspicious.

In FAST, a binned mean square error was computed as:

$$s^2 = \sum_{i=1}^{l} \frac{\left[\mathcal{N}_i - I_i(\hat{\mathbf{b}})\right]^2}{(l/m) I_i(\tilde{\mathbf{b}})} \qquad [5.43]$$

where $l = 64$ is the number of bins and m the total number of samples used. The statistic T was then computed as:

$$T = \sqrt{\frac{l-5}{2}}\left[\frac{s^2}{l-5} - 1\right] \qquad [5.44]$$

Under the null hypothesis, s^2 follows the chi-square distribution with $l - 5 = 59$ degrees of freedom and T approaches asymptotically the unit-normal distribution. The null hypothesis was rejected if $|T| > 3.5$, which happened in less than 0.5 per cent of all transits.

The Index *F*

In NDAC, a χ^2 value for the F statistic was derived for the binned mean counts, assuming them to be stationary:

$$\chi^2 = \sum_{i=1}^{l} \frac{\left[(1/n_i)\sum N_{k|i} - \hat{b}_1\right]^2}{(1/n_i)\sum N_{k|i}} \qquad [5.45]$$

As for the T statistic, the χ^2 value was transformed into a pseudo-Gaussian variable, except that the number of degrees of freedom was $d = 11$.

In FAST the binned mean square of the estimated modulation components was computed as:

$$p^2 = \sum_{i=1}^{l} \frac{\left[I_i(\hat{\mathbf{b}}) - \hat{b}_1\right]^2}{(l/m)I_i(\tilde{\mathbf{b}})} \qquad [5.46]$$

having four degrees of freedom. The statistical index F was then defined as a Fisher ratio between the statistics in Equations 5.46 and 5.43:

$$F = \frac{p^2/4}{s^2/(l-5)} \qquad [5.47]$$

Since $l - 5$ was rather large, $4F$ almost followed a χ^2 distribution with four degrees of freedom. Accordingly, the null hypothesis was accepted (no modulation found) if $F < 4.5$. This happened in less than 1.5 per cent of all transits.

5.8. Veiling-Glare Correction by FAST

The purpose of the veiling-glare correction was to clean the five parameters of $\hat{\mathbf{a}}_j$ of programme star j from the possible perturbations of the intensity and phase estimates by brighter stars observed during the same frame. Such perturbations were due to the instantaneous field of view sensitivity all over the field of view.

The image dissector tube efficiency was taken from on-ground calibration and represented by 9 functions centred on 9 regularly distributed points of the grid. Each function was represented by 11 values given along radii every 30°. These values corresponded to distances to the centre expressed in arcsec such that their logarithm grows regularly from 1.5 to 4.0. The efficiency at a given point was computed by interpolating this three-parameter table using linear or quadratic interpolation formulae.

The most general way to implement the veiling-glare correction would have been to start from the observed data $(\hat{\mathbf{b}}_j, \mathbf{B}_j)$ for all transits in a frame, and directly estimate the corrected data $(\hat{\mathbf{a}}_j, \mathbf{A}_j)$. Under the following assumptions:

- veiling glare was only due to other programme stars observed in the same frame;
- all of the programme stars had the same motion component p_k across the slits at time t_k;
- the instantaneous field of view was properly centred for each observed star;

- the instantaneous field of view sensitivity profile $\Psi(\varrho)$ was perfectly known;

the resulting statistics would still have been sufficient. The basic formulae for correcting an observation j for the influence of a brighter observation l would have been the following:

$$\begin{aligned}
&\hat{a}_{1j} = \hat{b}_{1j} - f\hat{b}_{1l} \\
&\hat{a}_{2j} = \sqrt{(\hat{b}_{2j} - f\hat{b}_{2l})^2 + (\hat{b}_{3j} - f\hat{b}_{3l})^2}\,, \quad \hat{a}_{3j} = \arctan\left(-\frac{\hat{b}_{3j} - f\hat{b}_{3l}}{\hat{b}_{2j} - f\hat{b}_{2l}}\right) \\
&\hat{a}_{4j} = \sqrt{(\hat{b}_{4j} - f\hat{b}_{4l})^2 + (\hat{b}_{5j} - f\hat{b}_{5l})^2}\,, \quad \hat{a}_{5j} = \arctan\left(-\frac{\hat{b}_{5j} - f\hat{b}_{5l}}{\hat{b}_{4j} - f\hat{b}_{4l}}\right)
\end{aligned} \qquad [5.48]$$

where $f = \Psi(\varrho_{jl})$ is the instantaneous field of view attenuation factor depending on the angular separation of the two pointings.

In practice the above corrections would have been seriously affected by calibration uncertainties in the instantaneous field of view profile, which increased in relative terms as the value of f decreased. Since the veiling-glare corrections were proportional to $\Psi(\varrho)$, the quantity:

$$q = \frac{\mathrm{d}\ln\Psi(\varrho)}{\mathrm{d}\varrho}\,\sigma_\varrho$$

indicates the relative precision of the corrections, given an estimate of the standard deviation σ_ϱ, including uncertainties in instantaneous field of view positioning and star distance. Since $\mathrm{d}\ln\Psi(\varrho)/\mathrm{d}\varrho < 0.05$ arcsec^{-1} for $\varrho > 20$ arcsec, the veiling-glare correction could be effective also with σ_ϱ around 2 arcsec.

The procedure adopted by FAST made the correction only when necessary and directly on the statistics $(\hat{\mathbf{a}}, \mathbf{A})$, which required more complex formulae than those presented above. The corrected phases $\hat{a}_3$ and $\hat{a}_5$ and the covariance matrix $\mathbf{A}$ were then used to estimate the reference phase g_0 and its variance σ_0^2 according to:

$$\hat{g}_0 = \hat{a}_3 + w(\hat{a}_5 - \hat{a}_3), \qquad \sigma_0^2 = (1-w)^2 A_{33} + w^2 A_{55} + 2(1-w)wA_{35} \qquad [5.49]$$

where w was defined by Equation 5.6, and A_{ik} are elements of the estimated covariance $\mathbf{A}$.

5.9. Optical Transfer Function Calibration and Three-Parameter Solution

The transit of a double or multiple component object consisted of the superposition of two or more signals as described by Equation 5.2 or 5.4. This changes the values observed for (μ, ν) or (β_4, β_5). For single stars, these values were a function of position in the field of view and of the colour of the star and were described by the optical transfer function. By calibrating the optical transfer function, it became possible to test the hypothesis that the transit was due to a single star only.

Calibration of the Optical Transfer Function

In NDAC, the calibration of the optical transfer function was done using the values for (μ, ν) or $(\beta_4,\ \beta_5)$ collected over one orbital period of the satellite. The successful

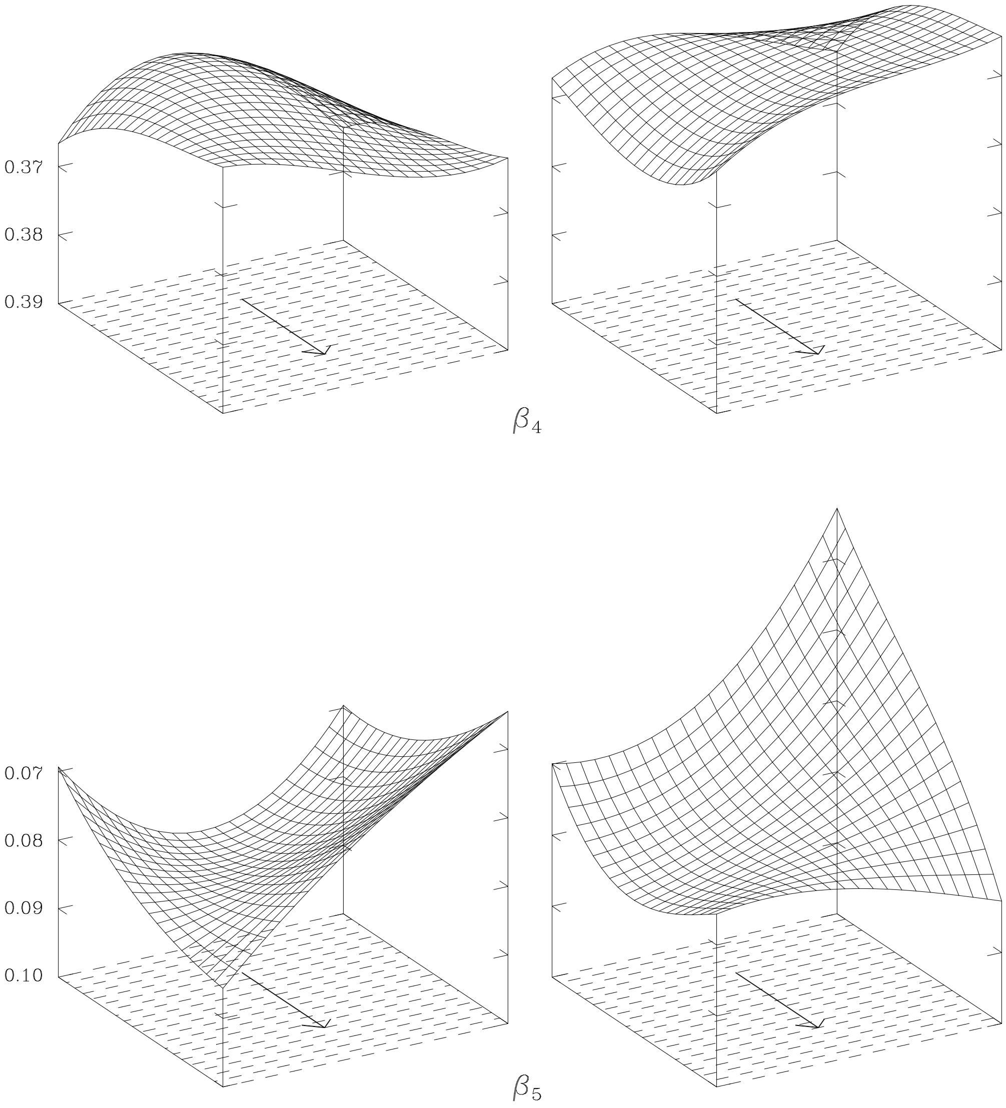

Figure 5.5. *The behaviour of β_4 and β_5 as a function of position in the field at the beginning of the mission. The scan direction is indicated by the arrow, the two graphs for β_4 and β_5 refer to the two fields of view. Scales for the two fields of view are identical.*

collection of data was always interrupted by the perigee passage of the satellite, where observing conditions were very poor and no ground station control was available over a period of 1 to 2 hours around perigee time. Thus, data collected during an orbit formed a natural unit for many calibrations.

The frame transit data was associated with a position on the grid (G, H) at mid-frame time, and with the colour index for the star observed. The calibration values obtained for stars not known or found to be double were modelled with a two-dimensional third-order polynomial in position, first and second order in colour index, and cross-terms between colour and position on the grid, 14 parameters in total. The calibrations were done independently for the two fields of view. Of the parameters, the positional dependence

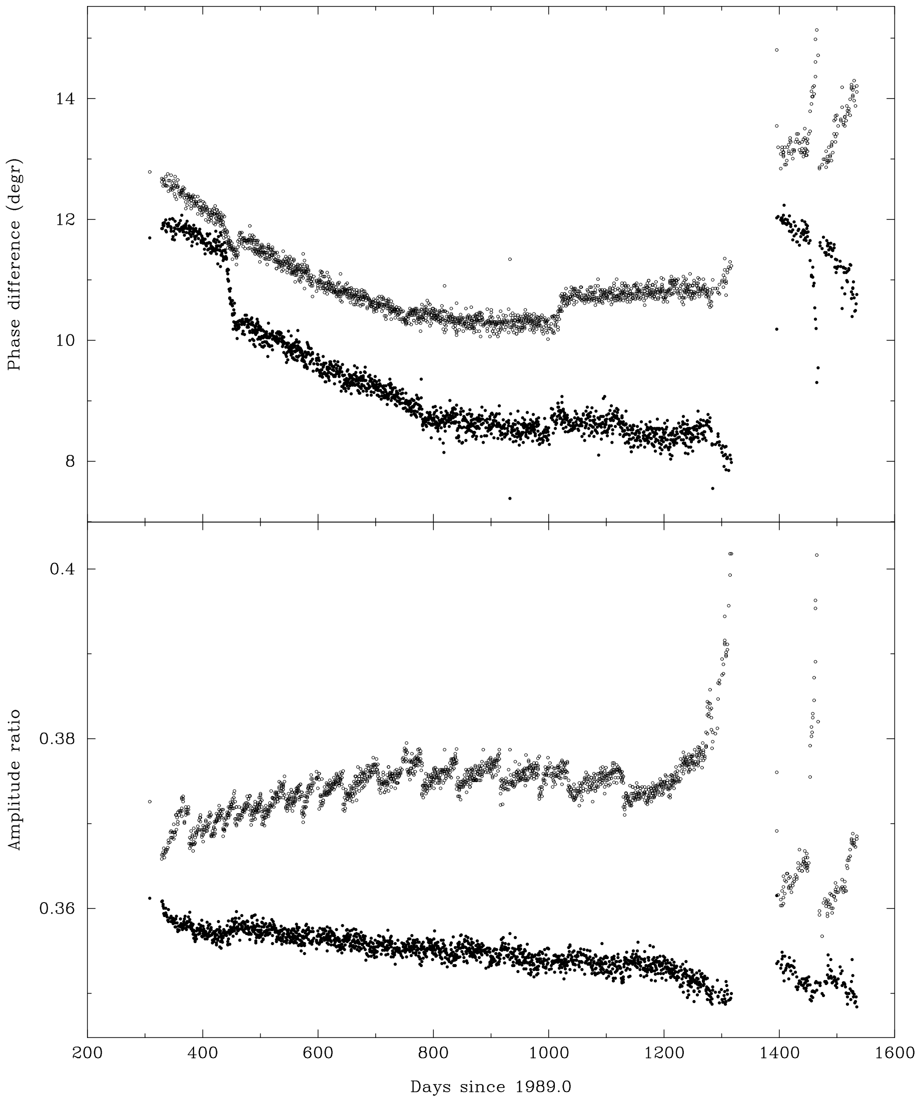

Figure 5.6. *Evolution with time of the phase difference ν and the amplitude ratio μ. Data for the preceding field of view are shown by filled symbols (points in the lower parts of the graphs), for the following field of view by open symbols (points in the upper parts of the graphs). Features in the top graph around days 450 and 1020 are related to variations in the satellite's exposure factor, shown in Figure 8.3.*

was the most important. An example of this dependence is shown in Figure 5.5. The calibration was time dependent, as shown in Figure 5.6, and affected by refocusing of the instrument. The colour dependence in the preceding field of view for β_4 increased during the mission by a factor 2, while for β_4 in the following field of view and for β_5 this dependence was much less a function of time. The amplitude ratio μ decreased towards redder stars, but could not be calibrated for the very red stars, as too few measurements were available. At $B-V=2$ the decrease was approximately 10 per cent in the following field of view, less in the preceding field of view.

In FAST, the calibration of the optical transfer function was, as were most calibrations, performed twice. For the image dissector tube data processing, the calibration was done in Utrecht by the 'First Look' task once a week. The mean for a calibration period (as defined in Chapter 4) was then made and used by the image dissector tube data processing as described in this chapter. In a second run, the five-parameter solutions obtained in this processing were used in a more refined analysis intended to be used by the multiple star and photometry tasks. About twenty orbits contributed to each calibration period, chosen from those giving the best results in the great-circle reduction.

The procedure was as follows. All the results of the five-parameter solution were examined and several tests performed in order to exclude known double stars, faint stars (magnitude > 11), stars with an unknown colour, and all stars for which either the ratio of the 'ac' to 'dc' photometry or the difference $a_3 - a_5$ suggested that the star was double. Additional rejections were made from the analysis of histograms of these quantities. The 'ac' intensity was computed and used to determine M_1 and M_2 from a_2 and a_4.

Each quantity M_1, M_2 and $a_3 - a_5$ for each field of view was expressed as a third-order polynomial in the grid coordinates G and H plus a similar polynomial multiplied by $C - 0.5$, where C is the colour index; this gave 20 parameters in total. The equations were solved by least-squares giving for each a weight proportional to the intensity of the star (a_1). An *a posteriori* rms was computed as two rms residuals of the colour independent part and of the colour dependent part.

In addition, the reference intensity response was calibrated for a mesh of 19×19 points on the grid for three classes of colours and also by a polynomial of the third order in G and H, second order in colour and some mixed terms.

The Three-Parameter Solution

In NDAC, the optical transfer function was applied to the (G, H) coordinates and star colour of each frame transit to provide predicted values for β_4 and β_5. These provided, together with the relevant elements of $\mathbf{B}_\beta^{-1}$, a χ^2 estimate for the likelihood of the signal being the result of one point source only:

$$\chi^2 = \delta\beta_4^2[\mathbf{B}_\beta^{-1}]_{44} + 2\delta\beta_4\delta\beta_5[\mathbf{B}_\beta^{-1}]_{45} + \delta\beta_5^2[\mathbf{B}_\beta^{-1}]_{55} \qquad [5.50]$$

where $\delta\beta_4$ is the difference between the observed and predicted value of β_4, and similarly for $\delta\beta_5$. The χ^2 values were collected per star for the purpose of double-star recognition. This was done using a transformation of χ^2 into a variable that has a flat distribution for single point-source objects, but becomes increasingly skew for disturbed objects:

$$c = 8\exp(-0.5\chi^2) \qquad [5.51]$$

where the factor 8 allowed the accumulation into eight discrete bins by taking the integer part of c as the index of the bin (from 0 to 7). A second criterion for detecting similar problem cases was derived from the photometric reductions and is described in Chapter 14.

In FAST the optical transfer function calibration allowed for the representation of the signal through the three-parameter model, Equation 5.5. For a true single star transit, the residuals $I_k(\hat{\mathbf{b}}) - I_k(\hat{\mathbf{r}})$ should be a zero-mean white noise, with the variance estimated by s^2 as in Equation 5.43. The statistical test used the Fisher ratio F_{35}:

$$F_{35} = \frac{p_{35}^2/2}{s^2/(l-5)} \qquad [5.52]$$

where:

$$p_{35}^2 = \sum_{k=1}^{m} \frac{\left[I_k(\hat{\mathbf{b}}) - I_k(\hat{\mathbf{r}})\right]^2}{I_k(\hat{\mathbf{b}})} \qquad [5.53]$$

was estimated from the residuals of Equation 5.5. Also, in this case, the Fisher variable $2F_{35}$ could be assumed to be asymptotically distributed as a χ^2 distribution having two degrees of freedom. The null hypothesis (single star) was rejected when $F_{35} > 3.5$. The F_{35} statistic became unreliable for stars of extreme colour, as these could not be included in the calibration model as described above.

5.10. Comparisons

Comparisons were carried out before launch using simulated data, and after launch in March 1991 using data from one orbit, covering roughly 11 000 frames and 50 000 individual transits. This comparison showed that differences in the reduction results between the two consortia were very small and in all cases negligible. The comparison exercise resulted in a relaxing of the instantaneous field of view pointing accuracy criterion in NDAC from 7 to 10 arcsec and a correction of the bias in the estimate of the first harmonic amplitude. Standard deviations of the differences between the phase estimates were well below the expected photon-noise level, showing that both consortia were producing results that were not significantly affected by any calibration or modelling errors: the noise remaining on the estimated parameters was primarily the result of the original photon noise on the counts, which was the same for both groups.

F. van Leeuwen, E. Canuto, F. Donati, J. Kovalevsky